AGU PUBLICATIONS

JGR

Journal of Geophysical Research: Solid Earth

RESEARCH ARTICLE
10.1002/2014JB011453

Key Points:
- Viscous sintering is a rapid process in hot glassy volcanic ash
- Nonisothermal viscous sintering is strongly nonlinear
- Sintering timescale is governed by melt viscosity and particle size

Correspondence to:
F. B. Wadsworth,
Fabian.wadsworth@min.uni-muenchen.de

Citation:
Wadsworth, F. B., J. Vasseur, F. W. von Aulock, K.-U. Hess, B. Scheu, Y. Lavallée, and D. B. Dingwell (2014), Nonisothermal viscous sintering of volcanic ash, *J. Geophys. Res. Solid Earth*, *119*, 8792–8804, doi:10.1002/2014JB011453.

Received 11 JUL 2014
Accepted 20 NOV 2014
Accepted article online 3 DEC 2014
Published online 20 DEC 2014

Nonisothermal viscous sintering of volcanic ash

Fabian B. Wadsworth[1], Jérémie Vasseur[1], Felix W. von Aulock[2], Kai-Uwe Hess[1], Bettina Scheu[1], Yan Lavallée[2], and Donald B. Dingwell[1]

[1]Department of Earth and Environmental Sciences, Ludwig Maximilian University, Munich, Germany, [2]School of Earth, Ocean and Ecological Science, University of Liverpool, Liverpool, UK

Abstract Volcanic ash is often deposited in a hot state. Volcanic ash containing glass, deposited above the glass transition interval, has the potential to sinter viscously both to itself (particle-particle) and to exposed surfaces. Here we constrain the kinetics of this process experimentally under nonisothermal conditions using standard glasses. In the absence of external load, this process is dominantly driven by surface relaxation. In such cases the sintering process is rate limited by the melt viscosity, the size of the particles and the melt-vapor interfacial tension. We propose a polydisperse continuum model that describes the transition from a packing of particles to a dense pore-free melt and evaluate its efficacy in describing the kinetics of volcanic viscous sintering. We apply our model to viscous sintering scenarios for cooling crystal-poor rhyolitic ash using the 2008 eruption of Chaitén volcano as a case example. We predict that moderate linear cooling rates of > 0.1°C min^{-1} can result in the common observation of incomplete sintering and the preservation of pore networks.

1. Introduction

Investigations into the central role of viscous sintering and welding in the deposition of volcanic materials are widespread [e.g., *Castro et al*., 2012; *Quane and Russell*, 2005b; *Sparks et al*., 1999; *Stasiuk et al*., 1996; *Tuffen and Dingwell*, 2005; *Tuffen et al*., 2003; *Tuffen et al*., 2008; *Wright and Cashman*, 2014; *Wilding et al*., 1996]. Volcanic pyroclasts sinter and weld during hot subaerial aggradation in cinder cones [*Sumner et al*., 2005], in high-grade ignimbrites [*Branney and Kokelaar*, 2002; *Ragan and Sheridan*, 1972; *Smith*, 1960], within fractures filled with transiently granular magma [*Kolzenburg et al*., 2012; *Tuffen et al*., 2003] and even in the hot zone of jet engines [*Kueppers et al*., 2014; *Song et al*., 2014]. This process is common and occurs when the temperature of volcanic ash is above the glass transition interval such that the melt phase can relax and sinter viscously [*Vasseur et al*., 2013].

Upon deposition, an initially granular pack of volcanic ash particles contains a high fraction of interconnected pore volume. The transience of porosity during viscous sintering is evident in the large range of porosities [*Michol et al*., 2008; *Quane and Russell*, 2005b; *Wright and Cashman*, 2014] and pore textures [*Quane and Russell*, 2006; *Tuffen and Dingwell*, 2005] recorded in variably welded deposits. Such transience of highly connected pore networks has implications for outgassing efficiency. This is expressed through the evolution of permeability, which exerts a first-order control on the longevity of gas overpressure in volcanic conduits [*Klug and Cashman*, 1996; *Mueller et al*., 2005] and thereby the propensity of the magma contained therein to fragment [*Mueller et al*., 2008]. Moreover, there is a strong dependence of the dynamic tensile strength of magma on porosity, and therefore, the sintering process must influence the threshold of failure in deforming magmas [*Vasseur et al*., 2013]. Despite the potential impact of the above, the time dependence of porosity, relative density, and permeability are poorly constrained over the wide spectrum of densification processes active in volcanic environments.

Viscous sintering—commonly referred to as *welding* in volcanology—involves the transition from an initially granular material with a melt component to a dense suspension of phases in melt. It can occur rapidly under volcanic conditions [*Quane and Russell*, 2005a; 2006; *Quane et al*., 2009; *Russell and Quane*, 2005]. Experiments in material science have yielded a range of physical models for the sintering process [*Frenkel*, 1945; *Mackenzie and Shuttleworth*, 1949; *Olevsky*, 1998; *Scherer*, 1977; *Uhlmann et al*., 1975] including the effects of cosintering crystallization [e.g., *Prado et al*., 2003], application of external loads [e.g., *Rahaman et al*., 1987; *Scherer*, 1986], and the inclusion of purely elastic particles on the sintering dynamics [e.g., *Mueller et al*., 2007; *Pascual et al*., 2005]. These models provide a basis for the application of sintering theory to volcanic settings. Key differences nevertheless remain, resulting from further complexities of volcanic materials. Fragmental

volcanic liquids degas [e.g., *Castro et al*., 2005b; *Stevenson et al*., 1997], resulting in time-dependent melt viscosities [*Hess and Dingwell,* 1996]; they may be compositionally variable (e.g., banded) on a wide range of scales [e.g., *Castro et al*., 2005a], they may exhibit surface crystallinity [*Ayris et al*., 2013], and they are often deposited in complex atmospheres of volcanic gases [*Sigurdsson et al*., 1999] that can variably resorb upon cooling [*Sparks et al*., 1999]. Moreover, the temperature conditions during deposition (and sintering) do not remain constant. Volcanic materials ultimately cool to ambient conditions [*Gottsmann and Dingwell,* 2002]; yet heat may be generated via a number of mechanisms along the way. Such heat can be readily produced through viscous heating [*Cordonnier et al*., 2012], granular friction [*Lavallée et al*., 2014], magma injection, and crystallization [*Applegarth et al*., 2013]. Therefore, the adaptation of sintering models to volcanic conditions is not necessarily trivial, and further experimental constraints are warranted. Here a combined analytical and experimental approach is used to explore the kinetics of sintering under nonisothermal conditions leading to a versatile model applicable to a diverse range of volcanic environments.

2. Theoretical Framework

2.1. Isothermal Viscous Sintering

Viscous sintering of melt particles is traditionally envisaged as a multistage process whereby packed granular particles form necks with neighbors, evolving to a melt-supported suspension with a variably connected pore network and finally to a dense, pore-free melt [*Frenkel*, 1945; *Mackenzie and Shuttleworth*, 1949]. The stress in these models is the surface stresses resulting from interfacial tension.

As described by *Frenkel* [1945], the initial stage of sintering of an isotropic packing, in which viscous necks form between melt particles of initial radius r_i, can be cast in terms of either a linear shrinkage (strain) S of a bulk sample with initial length L_i that undergoes a change in length ΔL

$$S = \frac{\Delta L}{L_i} = \frac{3\Gamma}{8\mu r_i} t \tag{1}$$

or the temporal evolution of the relative density: $\rho_r = \rho/\rho_m$ where ρ is the time-dependent packing density and ρ_m is the melt density. The *Frenkel* [1945] model is

$$\rho_r = \rho_{r,i}\left(1 - \frac{3\Gamma}{8\mu r_i} t\right)^{-3} \tag{2}$$

for which $\rho_{r,i}$ is the initial relative density, μ is the Newtonian melt viscosity, Γ is the interfacial tension at the melt-vapor surface, and t is the time. Equations (1) and (2) have been shown to describe well the initial evolution of viscously sintering tight packs of materials in the absence of crystallization [e.g., *Scherer and Bachman*, 1977]. Variations on the theory of Frenkel have been used to discriminate early stage sintering mechanisms by viscous flow or volume diffusion but are inadequate for describing more complex surface diffusion sintering processes often involved in neck formation [e.g., *Kingery and Berg*, 1955].

The neck formation stage of viscous sintering is empirically constrained to be complete at a relative density of 0.75–0.85 (depending on the initial packing type [*Prado et al*., 2001]) at which point, the granular packing hosts a continuous melt phase suspending both isolated and interconnected pores. The physical argument for the point at which the neck formation stage is complete is empirical and remains so poorly defined that some authors argue for a continuum model neglecting this stage altogether [*Olevsky*, 1998; *Vasseur et al*., 2013]. The remainder of the transition to a fully dense melt proceeds by the relaxation of the internal surface area of the pore network [*Mackenzie and Shuttleworth*, 1949] which was shown to be well approximated by [*Chiang et al*., 1997; *Prado et al*., 2001]

$$\frac{\mathrm{d}\rho_r}{\mathrm{d}t} = \frac{3\Gamma}{2a_i\mu}(1 - \rho_r) \tag{3}$$

where a_i is the radius of the suspended pores which, depending on the initial particle packing type, is a function of r_i. This model approximates a connected network of gas volume as a packing of shrinking spherical bubbles whose number remains constant and who do not interact with one another. Integration of equation (3) results in

$$\rho_r = 1 - \left(1 - \rho_{r,i}\right)\exp\left(-\frac{3\Gamma}{2a_i\mu} t\right) \tag{4}$$

Prado et al. [2001] further proposed a continuum model in which the process is predicted to transition smoothly from the neck formation regime to the pore network relaxation regime for a polydisperse packing of initial particles such that

$$\rho_r = \sum_r [\rho_1(r,t)\theta_1(t_\alpha - t) + \rho_2(r,t)\theta_2(t - t_\alpha)]\phi_r\xi_r \tag{5}$$

where ρ_1 and ρ_2 are the densities of the packing in the neck formation and pore-shrinking regimes, respectively. Here r is a particle radius bin in a measured distribution of radii. The step functions, θ_1 and θ_2 switch between values of 0 and 1 to operate the transition from one regime to the next at critical time t_α. This time (t_α) occurs when the critical relative density ρ_α at the end of the neck formation stage is reached such that at $t < t_\alpha \equiv \rho(r,t) < \rho_\alpha$ and the dynamics are governed by equation (2), otherwise at $t > t_\alpha \equiv \rho(r,t) > \rho_\alpha$ and the dynamics are governed by equation (4). Explicitly, $\theta_1 = 1$ and $\theta_2 = 0$ at $t < t_\alpha$ and $\theta_1 = 0$ and $\theta_2 = 1$ at $t > t_\alpha$. ϕ_r is the volume fraction of particles with radius r. It should be noted that equations (1) and (3) were developed for monodisperse packs of spheres, and therefore, it is an approximation to use equation (5) for different packing types of polydisperse particles. However, studies have verified the efficacy of a polydisperse approximation to monodisperse theory within analytical error and over ranges of particle size distributions similar to those used here [*Lara et al*., 2004; *Soares et al*., 2012].

The polydisperse result is parameterized in terms of the nondimensional function ξ_r which takes account of the number of particles n of any radius that form a neck with a particle of radius r. ξ_r is therefore an average of the number of necks that particles can form with any particle of a radius considered in the distribution of radii

$$\xi_r = \frac{1/r^c}{\sum_r \phi_r/r^c} \tag{6}$$

where the exponent c is given by

$$\ln \sum_k n(r, r_k)\phi_{r_k} = \beta - c\ln(r) \tag{7}$$

for which β is an inconsequential constant and $n(r, r_k)$ is the number of particles of radius r that can be accommodated around a particle of radius r_k. *Prado et al*. [2001] showed that for spherical particles the following is an approximate solution for n

$$n \approx \frac{2\pi}{\sqrt{3}}\left[\frac{2}{3} + 2\frac{r_k}{r} + \left(\frac{r_k}{r}\right)^2\right] \tag{8}$$

Ensuring continuity between the dynamics of equations (2) and (4) via equation (5) is not trivial and requires a method for the calculation of a_i from the measurable initial particle radius r_i. *Mueller et al*. [2007] relate the linear shrinkage rate of *Frenkel* [1945] to the relative densification rate of *Mackenzie and Shuttleworth* [1949] as follows

$$\frac{dS}{dt} = \frac{\rho_{r,i}^{1/3}}{3\rho_r^{4/3}}\frac{d\rho_r}{dt} \tag{9}$$

which yields a method for estimating a_i at the transition relative density ρ_α between the two sintering regimes such that

$$a_i = \frac{4r_i}{3}\frac{\rho_{r,i}^{1/3}(1-\rho_\alpha)}{\rho_\alpha^{4/3}} \tag{10}$$

2.2. Nonisothermal Viscous Sintering

Subject to a linear heating rate q, nonisothermal conditions permit the conversion of time t to temperature T by $dt = dT/q$. With this consideration we can integrate the temperature T between the glass transition temperature T_g (we use the onset of T_g measured at 10°C min^{-1} in both the model and experiments) and the experimental temperature T and time t, which leads to a nonisothermal model of viscous sintering. Equation (1) becomes

$$\rho_r = \rho_{r,i}\left(1 - \frac{3\Gamma}{8r_i q}\int_{T_g}^{T}\frac{1}{\mu}dT\right)^{-3} \tag{11}$$

Table 1. Composition of Materials

Oxide	Glass Beads (wt %)	DGG (wt %)
SiO_2	72.50	71.72
TiO_2	0.00	0.14
Al_2O_3	0.40	1.23
Fe_2O_3	0.20	0.19
MgO	3.30	4.18
CaO	9.80	6.73
Na_2O	13.70	14.95
K_2O	0.10	0.34
SO_3	0.00	0.44
Total	100.00	99.91

and integrating between the temperature reached by time t_α, termed T_α, and the experimental temperature T, equation (3) becomes

$$\rho_r = 1 - (1 - \rho_{r,i})\exp\left(-\frac{3\Gamma}{2a_i q}\int_{T_\alpha}^{T}\frac{1}{\mu}\mathrm{d}T\right) \quad (12)$$

By applying the step-function principle in equation (5) to the nonisothermal case, we can solve for the continuum viscous sintering process in a maximum packing of polydisperse spheres during constant linear heating above the glass transition temperature. As previously mentioned, the relative density at which the transition from neck formation to pore shrinkage occurs is poorly constrained. It is empirically thought to occur at a relative density of 0.8.

3. Material Properties and Experimental Methods

Volcanic ash is typically produced by the brittle fragmentation of magma during which melt is subjected to stresses at rates which engender its glassy response [*Dingwell*, 1996]. This ash can then be sintered in a number of emplacement scenarios. In order to test the process of sintering in complex, nonisothermal conditions we employ here a standard glass whose physical properties are analogous to volcanic glass. We have chosen to use a viscosity standard (soda-lime glass; Table 1) from the Deutsche Glastechnische Gesellschaft (DGG) as it has precisely determined thermal properties including glass transition and liquidus temperatures, a well-constrained temperature dependence of viscosity, and its excellent glass-forming ability (i.e., its kinetic reluctance to crystallize, degas, or exhibit liquid-liquid immiscibility) at our experimental temperatures and timescales. Additionally, we use populations of solid spherical soda-lime silica (Table 1) Spheriglass® glass beads. We predict the temperature dependence of viscosity of the melt derived from the glass beads by using the multicomponent model of *Fluegel* [2007] developed for industrial glass-forming silicate melts. This composition-dependent model is in excellent agreement with the viscosity measurements of *Okhotin and Tsoi* [1952] using a glass of near-identical chemical composition (Figure 1).

The DGG glass was powdered in an acetone ball mill for ~1 h. The particle size distributions of both the powdered DGG glass and the glass beads were measured using a Coulter LS230 laser refraction particle size analyzer with a measuring range 0.375–2000 μm (Figure 2). The particle size distribution of both the glass beads and the DGG glass powder used are monomodal and range between 10^0 and 10^2 μm. The DGG glass powder consists of angular fragments whereas the glass beads are near spherical (Figure 2). The measured particle size distributions yields a linear relationship between ln(*r*) and the left side of equation (7) and therefore gives the *c* exponent used to predict the neck-forming ability of the polydisperse population. We find that for the glass beads, which have a dominant peak that is near-Gaussian, the value of *c* can be taken as ~1. This is in agreement with previous studies that have used this parameter with tightly clustered particle size distributions [*Lara et al.*, 2004; *Prado et al.*, 2001; *Soares et al.*, 2012].

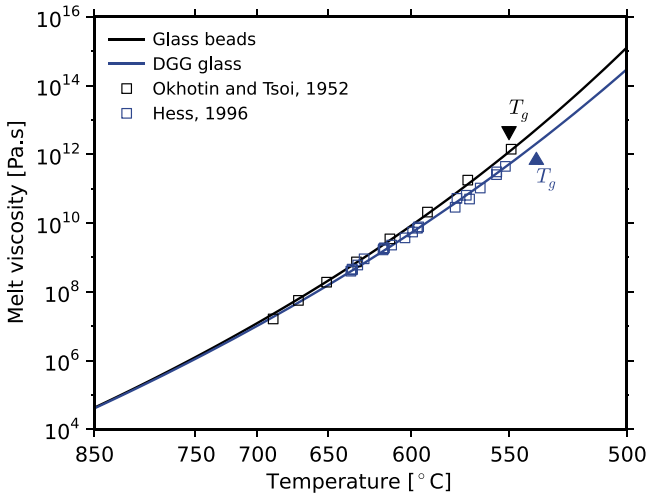

Figure 1. The temperature dependence of melt viscosity of the glass beads calculated after the composition-dependent model of *Fluegel* [2007] and of the DGG viscosity standard glass using the equation from *Hess* [1996] (Table 2). The glass transition temperature, T_g, is determined for a rate of 10 K min^{-1}.

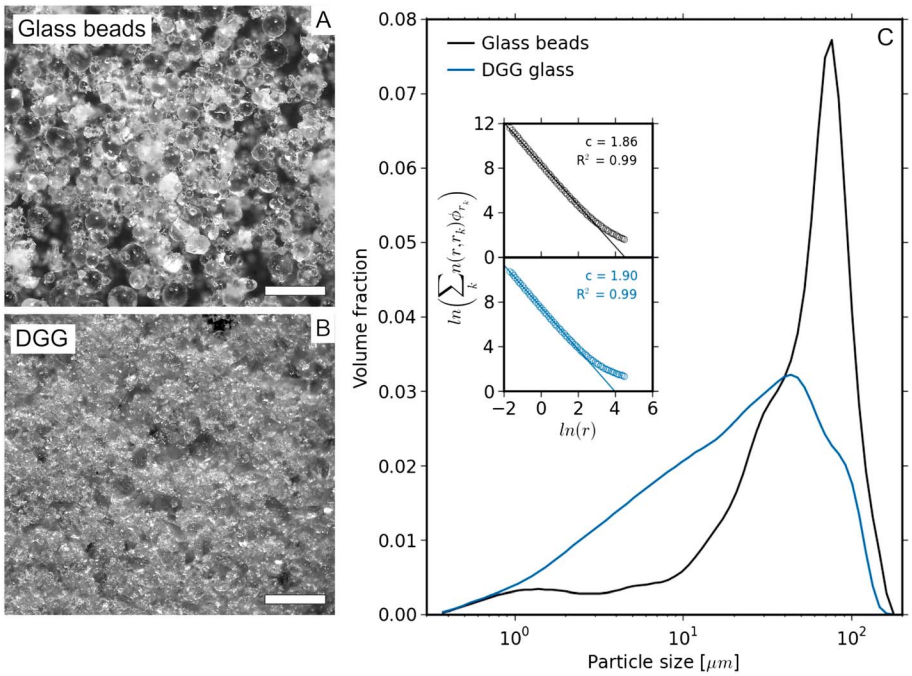

Figure 2. The experimental materials used in this study. (a) The glass beads and (b) powdered DGG viscosity standard glass. (c) The particle size distribution of the experimental materials. Inset: the result of calculating the parameter *c* from equation (7).

The onset of the glass transition (T_g) interval and the temperature dependence of the sample mass of the glass beads were measured simultaneously using a Netzsch simultaneous thermal analysis Jupiter 449 F1 (Figure 3). 56–83 mg samples were placed in lidded platinum crucibles (with holes) and heated at 5–30°C min^{-1} to 650°C in the presence of a 20 mL min^{-1} argon flow. We can thereby confirm that the glass bead material is stable over the experimental timescales and temperatures. The mass loss is negligible over multiple heating cycles (Figure 3c), and the onset of the glass transition T_g varies insignificantly (1 K) in successive measurements indicating that there is no change in the melt structure (Figure 3a inset). The heat flow data contain no evidence for exothermic crystallization peaks in the experimental temperature range.

Viscous sintering and the resultant densification rate can be characterized in situ with hot-stage microscopy [*Lara et al.*, 2004; *Soares et al.*, 2012; *Song et al.*, 2014]. We have used an EM201 Hesse Instrument hot stage at the Technical University of Munich [see *Boccaccini and Hamann*, 1999]. We formed ~3 mm diameter cylinders of packed particles for each experimental material, applied a linear heating rate of 1–36°C min^{-1} to 1500°C in argon at atmospheric pressure, and measured the temperature- and rate-dependent changes in sample cylinder height *L* and diameter *D*. Up to ~800–850°C (T_{end}; Figure 4) cylindrical geometry was maintained. As long as cylindrical geometry is maintained, *L* and *D* can be converted to a cylindrical volume *V*, and thus a sample bulk density via $\rho = M/(4/3\pi(D/2)^2 L)$ using the sample mass *M*. Additionally, we use the method of *Soares et al.* [2012] to convert the continuous measurements of height and diameter (Figures 4a and 4b) into relative densities (Figures 4c and 4d). The measurements of sample geometry are automated, and thus, the thermal expansion of the alumina substrate (~99.5 wt % Al_2O_3) is considered when deriving absolute changes in sample height.

The absolute volumes and densities at T_{end} were corroborated by conducting experiments in a furnace. Samples were exposed to linear heating rates and removed at temperature intervals to assess their geometry and density. The thermal expansion of the melt phase is negligible [*Bagdassarov and Dingwell*, 1992] within the analytical error on the measurement of sample geometry and over the range of volume changes associated with sintering (>40%) and is thus not considered further here. The absolute value of surface tension in silicate melts is negligibly temperature dependent over the range of temperature used here [*Gardner and Ketcham*, 2011, *Bagdassarov et al.*, 2000], and therefore, we use a constant value of 0.3 N m^{-1} [*Vasseur et al.*, 2013].

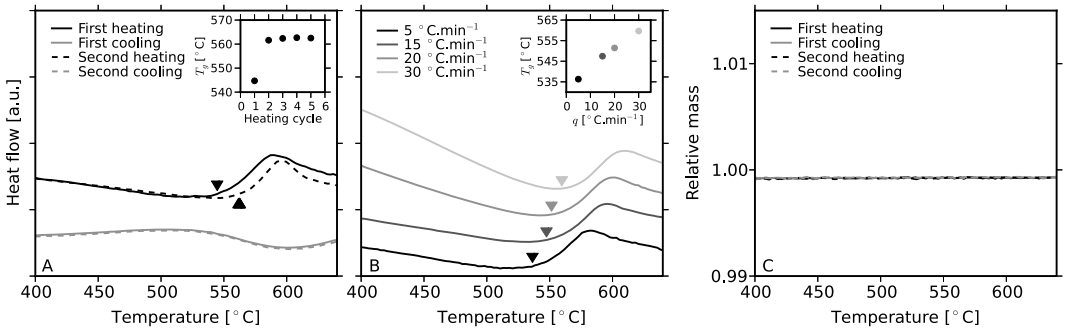

Figure 3. Thermal properties of the glass beads using a differential scanning calorimeter and thermogravimetry. (a) Heat flow over two identical heating cycles to 650°C at 10°C min^{-1}. Inset: the variation of the onset of T_g with repeated heating cycles showing that after the initial heating, the onset is stable. The initial heating cycle results in a low T_g due to the relatively slower cooling rate during the industrial glass formation process. (b) Heat flow at heating rates of 5, 10, 15, 20, and 30°C min^{-1} as used in the sintering experiments using fresh samples for each run. Inset: the relationship between heating rate and the measured onset of T_g (Table 2). (c) The temperature-dependent mass of a sample over two identical heating cycles to 650°C at 10°C min^{-1}. Thermal properties of DGG viscosity standard glass are known to be stable over the range of conditions used here and as such are not remeasured here.

4. Results

During heating in the hot stage, sample cylinders thermally expand by an amount (which is trivial for the present analysis) governed by their glassy thermal expansion coefficients until reaching the glass transition interval. As the glass transitions to a supercooled liquid, viscous deformation associated with internal surface relaxation begins and is manifested as isotropic shrinkage. No liquid-state expansion is observed after T_g,

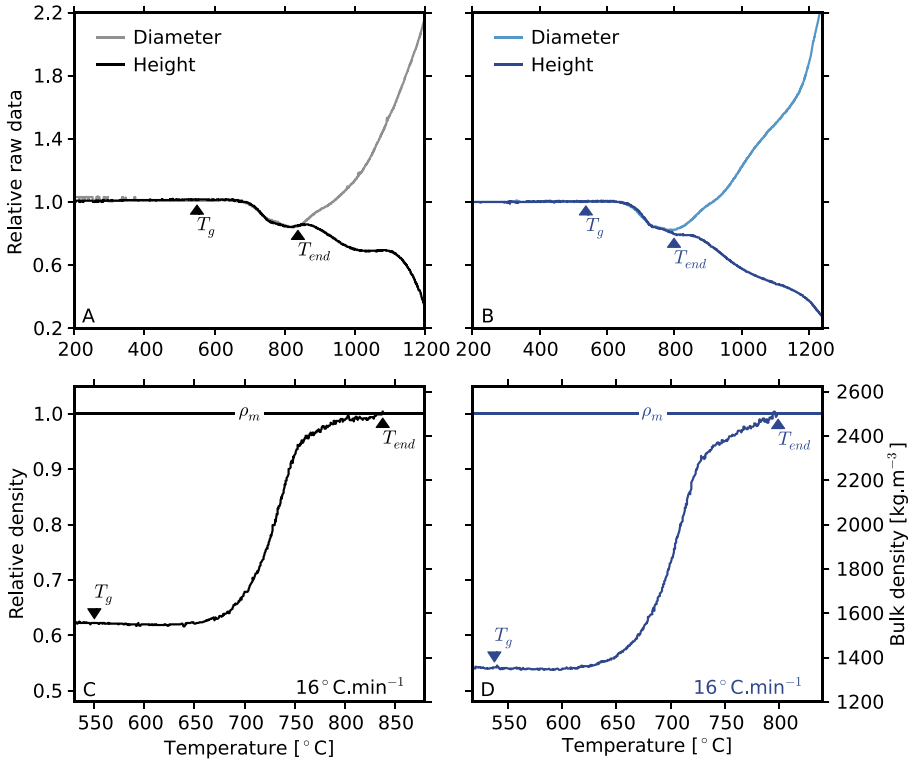

Figure 4. Results of densification of cold-pressed cylinders of maximally packed experimental materials in a hot stage showing the evolution of sample cylindrical height and diameter. (a, b) The results for the glass beads (black) and the DGG glass (blue) showing the change in sample height and diameter and indicating the range of temperatures over which cylindrical geometry is maintained. (c, d) The conversion of the data to bulk density.

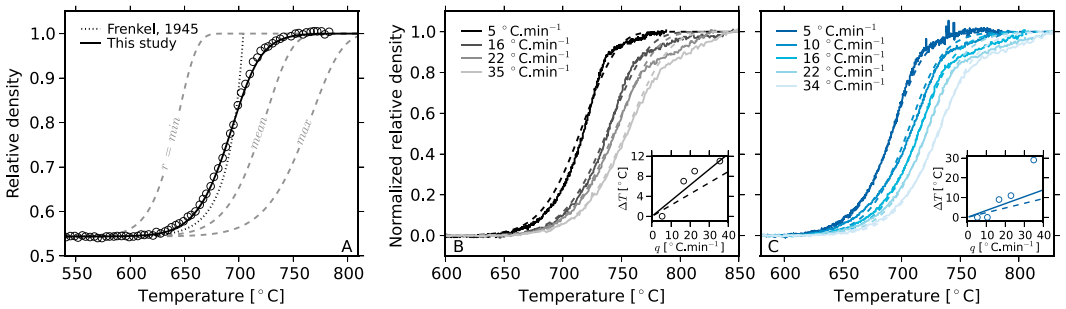

Figure 5. The normalized relative density curves over the range of temperature at which cylindrical geometry is maintained. Absolute initial and final densities are given in Table 2. The curves for the continuum model evolving from equations (11) to (12) are shown as dashed lines for each heating rate q considered. (a) The results for the 10 C min^{-1} experiment with glass beads showing the relative efficacy of different sintering models. (b) Results for the glass beads and (c) for DGG glass powder. Insets in Figures 5b and 5c show the values of ΔT used to correct the temperature data and model curves for the steady state ΔT in cylindrical samples with gas volume fractions of 0.4 (solid line) and 0 (dashed line).

suggesting that shrinkage dominates even at high melt viscosities. Typically, this is macroscopically seen at some point after the glass transition interval and has been termed "first shrinkage" [*Pascual et al.*, 2001]. The first shrinkage point occurs at higher temperatures when higher heating rates are applied. After the first shrinkage point, the sample length and diameter decrease approximately equally until the pore phase disappears. Once the density of the bulk sample is close to that of the melt phase (that is, once sintering is complete), the sample changes geometry and deviates from cylindrical upon further heating ($T > T_{end}$; Figure 4).

We find that the density of the samples relative to that of the melt phase increases from the first shrinkage point to a value of 1 regardless of heating rate (Figure 4). This indicates that negligibly small quantities of residual gas volume are suspended in the melt phase at the completion of sintering. Here this is likely a function of the small initial sample sizes and is not necessarily the case in larger sintering samples [e.g., *Vasseur et al.*, 2013].

5. Interpretation

5.1. Modeling Viscous Sintering Kinetics

Application of the analytical solution provided in section 2 to the experimental data set shows that our model accurately describes the continuous process from normalized relative densities of 0 to 1 at low heating rates. At higher relative densities and for higher heating rates, we note minor deviations as the observed densification rate is slower than predicted. However, given the large temperature and melt viscosity range over which our nonisothermal experiments are conducted, we find that the complete viscous sintering process is well resolved (to within 98%) by this polydisperse model for both the spherical glass beads and for the more angular DGG glass powder (Figure 5). We therefore conclude that minor angularity is a second-order effect compared with those effects that change the sintering timescale, namely, melt-vapor interfacial tension, viscosity, and particle size. To illustrate this, we show a single 5°C min^{-1} experiment for the DGG glass with the results of a polydisperse neck formation model using equation (2) [*Frenkel*, 1945], a monodisperse pore-shrinkage model using equation (4), for the mean, minimum, and maximum particle sizes [*Mackenzie and Shuttleworth*, 1949], as well as the polydisperse pore-shrinkage model (Figure 5a). Additionally, we find that the pore-shrinkage model of *Mackenzie and Shuttleworth* [1949] is sufficient to describe the entire sintering continuum. In this case, the initial neck formation phase that is predicted by the theory of *Frenkel* [1945] is only used to find the pore size between clustered particles (equation (10)). This is in keeping with isothermal continuum approximations made for viscous sintering of pure melts [*Olevsky*, 1998; *Soares et al.*, 2012; *Vasseur et al.*, 2013]. The question as to why the neck formation stage is of negligible importance in our system remains unanswered and is possibly a function of the small particle sizes used here. If this is the case, then it is likely that the total shrinkage associated with neck formation is small compared with the shrinkage accommodated by pore shrinkage and as such can be neglected. However, because we use volcanically relevant melt viscosities and particle sizes, the use of the pore-shrinkage model is satisfactory for use with volcanic ash.

The form of the modeled densification curves is identical to the continuous measured data for each heating rate. However, in absolute temperature space, we find that a shift-factor ΔT is required to obtain a good fit

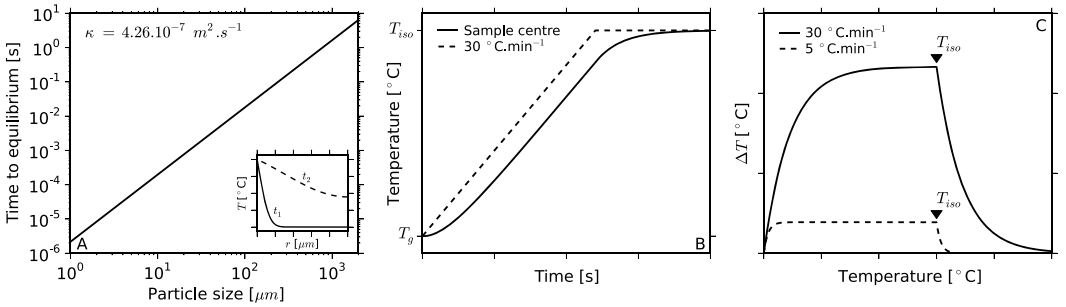

Figure 6. The results of a numerical solution of the 1-D heat equation for conductive heating of (a) an individual sphere in isothermal external conditions and (b) a cylindrical granular packing of spheres with a known initial porosity following the incorporation of porous insulating effects in nonisothermal conditions. (c) The modeled evolution of the maximum thermal gradient in the sample, ΔT, used to explain the discrepancy between the sintering model and the data at high heating rates (Figure 5).

athigh heating rates. At 5°C min^{-1}, the data remain unshifted, but at heating rates >5°C min^{-1} the ΔT required increases. We propose that the cause of this shift is the effect of thermal disequilibrium, and we therefore have to consider the rate of heat transfer in our samples.

5.2. Thermal Disequilibrium During Sintering

Under nonisothermal conditions, thermal disequilibrium in granular suspensions and in individual particles becomes a key consideration as differential sintering kinetics can result from melt viscosity gradients. Therefore, we provide an illustrative consideration of 1-D thermal conduction in (1) individual melt spheres and (2) cylindrical granular packs of spheres.

In spherical geometry with radius r, the heat equation is

$$\frac{\partial T}{\partial t} = \frac{\kappa}{r^2}\frac{\partial T}{\partial r}\left(r^2\frac{\partial T}{\partial r}\right) \text{with} \left\{ \begin{array}{l} T(r, t = 0) = T_i \\ T(r = R, t) = T_0 \end{array} \right\} \tag{13}$$

where κ is the thermal diffusivity and T_0 and T_i are the imposed and initial temperatures, respectively. By way of a Laplace transform, the general solution of this form of the heat equation for 1-D spherical geometry results in

$$\overline{T}(r, s) = \frac{T_0 - T_i}{s}\frac{R\sinh(\gamma r)}{r\sinh(\gamma R)} \tag{14}$$

for which $\overline{T}$ is the Laplace transform of temperature T, and $\gamma = \sqrt{s}/\kappa$ with s representing the Laplace parameter. A numerical solution to equation (14) yields the time-dependent evolution of temperature in a homogeneous sphere (Figure 6a). This shows that larger spherical volcanic ash particles take longer to reach thermal equilibrium when exposed to a new temperature condition. Homogeneous ash particles in the typical range of size fractions found in volcanic ash, 10^{-3}–10^{0} mm, will reach thermal equilibrium in 10^{-6}–10^{0} s for externally applied temperatures 600–800°C. Clearly, over this temperature range and at moderate heating rates, single ash size particles can be approximated as instantaneously equilibrated. This is not the case in packed granular mixtures in which, the thermal diffusion length scale is much smaller than the sample cylinder radius. Therefore, we also have to consider thermal equilibrium in packs of ash particles.

Adapting the 1-D heat equation to our 1.5 mm radius cylindrical samples being heated by a linearly increasing imposed surface temperature, analogous to our experimental set up, the differential equation is

$$\frac{\partial T}{\partial t} = \frac{\kappa}{r}\frac{\partial}{\partial r}\left(r\frac{\partial T}{\partial r}\right) \text{with} \left\{ \begin{array}{l} T(r, t = 0) = T_i \\ T(r = R, t) = qt \end{array} \right\} \tag{15}$$

where r is the spatial position normal to the axis of symmetry of the cylinder from a cylinder surface at R and q is the imposed heating rate. *Connor et al.* [1997] use a definition of the bulk thermal diffusivity in deposits that incorporates the differential thermal properties arising from significant gas volume fraction ϕ_g

$$\kappa = \frac{k}{\rho^m C_p^m(1 - \phi_g) + \rho^f C_p^f \phi_g} \tag{16}$$

Table 2. Properties of Materials

Parameter	Glass Beads	DGG
A_{VFT}	−2.6387[a]	−2.818[b]
B_{VFT}	4303.36[a]	4551[b]
C_{VFT}	530.754[a]	510.07[b]
$\rho^m{}_{800°C}$ (kg m^{-3})	2500	2500
$C_p{}^m$ (J kg^{-1} K^{-1})	880	1600
k^m (W m^{-1} K^{-1})	1.5	0.95
ρ_i (kg m^{-3})	1415–1613	1264–1375

[a] *Fluegel* [2007].
[b] *Hess* [1996].

where k is the thermal conductivity of the granular packing defined as $k = k^m[(1 - \phi_g)/(1 + \phi_g)]$ [*Bagdassarov and Dingwell*, 1994] and where k^m is the thermal conductivity of the melt. $C_p{}^m$ is the melt specific heat capacity, and ρ^m is the melt density. A superscript f in place of superscript m denotes the pore-fluid thermal properties. For simplicity, we consider equation (16) to be constant in space and time. We use thermal properties provided by the glass manufacturers of our experimental materials (Table 2).

As for the spherical case, a numerical solution to equation (15) using the finite difference method (the step size in space is 50 μm and in time is 2 ms) for a cylinder shows that in the case of a linearly increasing external temperature, a steady state is reached where the absolute temperature difference between the sample margin and the sample core is constant. The time to reach the constant temperature difference, ΔT, is dependent on the heating rate (Figure 6c).

Because we find that the continuum sintering model well predicts low heating rate experiments but is offset in absolute temperature from high heating rate experiments, we use this predicted temperature difference to correct the absolute temperature of the experimental data. This results in a measured ΔT which we compare with the calculated ΔT (Figure 6b inset). We find excellent agreement between the calculated and measured ΔT for the glass bead experiments but an offset at the highest heating rates for the angular DGG powder (Figure 6c inset).

5.3. Nondimensional Analysis

Nondimensionalization of temperature during linear heating can be achieved by $T_* = (T - T_g)/q\lambda$ where T_* is the specific nondimensional temperature and λ is the timescale of the *Mackenzie and Shuttleworth* [1949] pore-shrinkage sintering process such that $\lambda = 2a_i\mu/3\Gamma$. In Figure 7 we show the efficacy of our model over the range of heating rates considered by presenting a master sintering curve for all viscous sintering of metastable single phase melts.

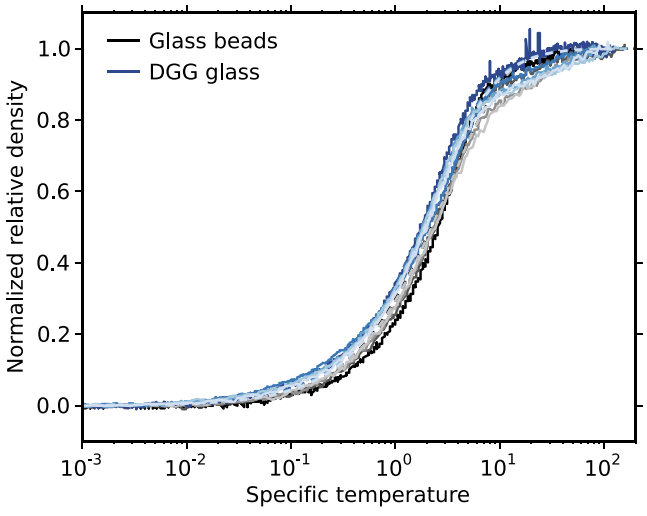

Figure 7. A master sintering curve showing the common behavior of sintering packs of melt grains when the nonisothermal temperature is normalized to the specific temperature (see text) over a range of heating rates and using two materials with different temperature dependencies of viscosity, glass transition temperatures, and grain size distributions.

5.4. Sintering in Volcanic Environments

We show that in nonisothermal conditions the transience of porosity is strongly nonlinear and can be well described by accounting for the effect of polydisperse grain size distributions and the variable melt viscosity.

In nature, volcanic ash involved in welding is deposited hot and/or external heat sources raise the temperature. Our model implies that above the glass transition, melt in volcanic ash will sinter viscously. Deposits that record some sintering, such as those found in welded ignimbrites [e.g., *Andrews and Branney*, 2011] and tuffisites [e.g., *Tuffen and*

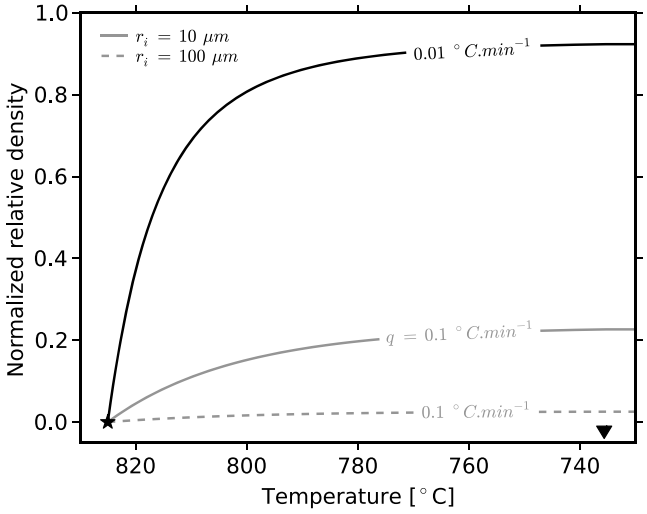

Figure 8. Consideration of nonisothermal viscous sintering at Chaitén Volcano using parameters from *Castro and Dingwell* [2009] to illustrate the application of the model presented. The starting relative density is 0.6. Curves are shown for 0.01 and 0.1 mm closely packed melt grains sintering under no external load under a linear cooling profile of 0.1°C min^{-1} from 825°C to T_g at 735°C. A constant dissolved water content of 0.1 wt % is considered for simplicity. Note that maximum density is not achieved before the temperature cools through the glass transition and viscous sintering ceases. The relative density at T_g is 0.69 and 0.61 for an r_i of 0.01 and 0.1 mm, respectively.

Dingwell, 2005], are commonly ranked according to one of several metrics that is considered to be time dependent in the sintering process, such as porosity, density, or strength [*Grunder and Russell*, 2005; *Grunder et al*., 2005; *Quane and Russell*, 2005b; *Wright and Cashman*, 2014]. Traditional field descriptors of welding include "nonwelded," "incipiently welded," "moderately welded" or "densely welded" [e.g., *Ross*, 1960; *Smith*, 1960; *Smith and Bailey*, 1966]. However, even if we think of a hot deposit of volcanic ash as isothermal, then it is clear from our results that a universal ranking for all deposits does not necessarily mean one can extrapolate to the timescale of the sintering process without considering the effect of grain size and temperature.

Natural volcanic materials are rarely deposited isothermally. Cooling occurs during adiabatic ascent, conductive and convective cooling, fragmentation, particulate transport, and postdeposition. Similarly, heating can occur by internal friction during viscous flow [*Cordonnier et al*., 2012], including strain localization [*Lavallée et al*., 2014] and conductive heating during deposition of subsequent hot material. Therefore, any scenario in which welding or sintering textures are used to infer timescales is dependent on the cooling or heating rates involved.

In the 2008 eruption of Chaitén Volcano the granular volcanic material preserved in tuffisite veins is often low crystallinity [*Castro et al*., 2012] as is the case in our experiments. Thus, if we apply our model to a sintering tuffisite vein at Chaitén, and if we use the polydisperse grain size distribution measured for our DGG glass powder (Figure 2), then we would predict that at a constant eruptive viscosity of $10^{9.95}$ Pa s (at 825°C and 0.1 wt % H_2O; values from *Castro and Dingwell* [2009] using the viscosity model of [*Hess and Dingwell*, 1996]), the isothermal sintering to zero porosity would be achieved after 10^5 s (~30 h). Given that tuffisite veins are often interpreted to represent degassing pathways in rhyolite volcanoes [*Schipper et al*., 2013], considerations such as these have implications for the longevity of porous channels at depth in volcanic conduits.

Using the same example of a tuffisite emplaced in hot Chaitén magma, we can model the predicted time evolution of bulk density when the system is allowed to cool to the glass transition. A minimum melt viscosity of 10^6 Pa s can be predicted using the model of *Hess and Dingwell*, [1996] and is for a magma temperature of 825°C and water content of 4 wt % (storage conditions prior to the 2008 eruption of Chaitén [*Castro and Dingwell*, 2009]). The maximum viscosity is for the temperature of the glass transition onset of 710°C with 0.1 wt % dissolved H_2O at a cooling rate of 10°C min^{-1}, giving 10^{12} Pa s [*Hess and Dingwell*, 1996]. The isothermal sintering timescale for the viscosity range between magmatic and glass transition temperatures (10^6–10^{12} Pa s) varies 10^1–10^7 s and 10^2–10^8 s for 0.01 and 0.1 mm particle sizes, respectively. If cooling occurs linearly over that same range from the eruptive temperature to the glass transition, then, according to our model using a grain size of 0.01 or 0.1 mm, a maximum relative density is reached by the time the material cools through the glass transition and viscous sintering stops (Figure 8). One can see that the effects of nonisothermal sintering make it challenging indeed to extrapolate from observed textures to densification timescales. The significant range of isothermal timescales involved demand good constraints on the dominant parameters such as cooling rate, initial volatile content, devolatilization kinetics, and initial grain size.

As stated, the volcanic system differs from homogeneous glass systems with time-independent physical properties. One key difference is that melts in magmas degas volatiles which induces melt viscosity gradients [*Hess and Dingwell,* 1996] and time dependency. Viscous sintering rates are likely retarded during the degassing process because water loss and the subsequent increase in melt viscosity will be greatest at the ash grain surfaces, which are where the driving stress for sintering is concentrated. Similarly, influx of water into the melt will accelerate sintering. The interplay between diffusional processes and the internal evolution of the occluding pore network surfaces is poorly constrained and is surely critical to volcanic environments.

We have presented here a first-order constraint on the effect of cooling rate and grain size; however, in nature, local stress conditions may contribute to sintering. Viscous sintering under either an isotropic confining pressure or a deviatoric stress will likely modify the densification timescale and dynamics. This additional complexity has been explored using volcanic materials [*Quane and Russell*, 2005a; *Quane et al*., 2009] over a range of uniaxial-applied loads relevant for shallow volcanic interiors. For a given material at a given temperature, the rate of densification is accelerated by loading. This echoes the findings of those who have investigated the pressure sensitivity of sintering in pure glasses [e.g., *Rahaman et al*., 1987; *Scherer*, 1986]. Under these conditions, the densification mechanics are less likely to be dominated by the effects of surface tension and more likely to be related to self-compaction under gravity [*Bercovici et al*., 2001; *Michaut et al*., 2009] or with densification associated with high shear strain [e.g., *Okumura et al*., 2010]. Under these varied conditions, effects such as shear localization [*Lavallée et al*., 2013], volatile resorption [*Sparks et al*., 1999], and porosity redistribution [*Laumonier et al*., 2011] will likely cause further complication of simple densification models.

Most silicic volcanic eruptions are thought to occur when pore overpressure exceeds a strength criterion for magma [*Gonnermann and Manga*, 2003; 2007; *Spieler et al*., 2004]. The nonlinear kinetics of nonisothermal sintering, even under the surface tension end-member, are critical to this process as the strength of magmas is modified by sintering densification [*Kolzenburg et al*., 2012; *Quane and Russell*, 2003; *Vasseur et al*., 2013]. In future, a time-dependent strength model for magma and the kinetics of sintering should be incorporated into conduit flow models for better analyses of the effects of pore overpressure developed during ascent or following decompression events.

6. Concluding Remarks

Under isothermal conditions, viscous sintering is strongly particle size and melt viscosity dependent with a weak dependence on the melt-vapor interfacial tension in silicate melts. In the more complex nonisothermal sintering scenario, the heating or cooling rate has the combined effect of introducing thermal disequilibrium in volcanic ash deposits, shifting the kinetic glass transition temperature interval, below which sintering progresses more slowly and diffusively, and affecting the rate of viscosity change and thus the rate of change of the sintering timescale. The range of particle angularities here investigated did not impact the sintering dynamics such that one model describes both spherical and angular glass particles. These considerations should be included in sintering and welding models for volcanic deposits. The model we present can be used as a tool for volcanologists to infer the longevity of statically sintering hot volcanic ash deposits.

Acknowledgments

We are grateful for comments from two reviewers who improved the manuscript. We thank Andrea Hartung at the hot-stage facility at the Technical University, Munich, for analytical assistance, Jenny Schauroth for help with image acquisition and Wenjia Song, Viviane O. Soares, Raphael Reis, Miguel Oscar Prado, and David E. Damby for fruitful discussion. We thank Adele Adkins for consistent help throughout. We acknowledge funding provided by the European Union's seventh program for research, technological development, and demonstration under grant agreement 282759 (VUELCO), the Deutsche Forschungsgemeinschaft (DFG) grant LA2651/3-1, and the European Research Council Starting grant (Strain Localisation in Magmas (SLiM, 306488)) and Advanced grant (Explosive Volcanism in the Earth System: Experimental Insights (EVOKES, 247076)).

References

Andrews, G. D. M., and M. J. Branney (2011), Emplacement and rheomorphic deformation of a large, lava-like rhyolitic ignimbrite: Grey's Landing, southern Idaho, *Geol. Soc. Am. Bull.*, *123*(3–4), 725–743.

Applegarth, L. J., H. Tuffen, M. R. James, and H. Pinkerton (2013), Degassing-driven crystallisation in basalts, *Earth Sci. Rev.*, *116*, 1–16.

Ayris, P., A. Lee, K. Wilson, U. Kueppers, D. Dingwell, and P. Delmelle (2013), SO_2 sequestration in large volcanic eruptions: High-temperature scavenging by tephra, *Geochim. Cosmochim. Acta*, *110*, 58–69.

Bagdassarov, N., and D. Dingwell (1994), Thermal properties of vesicular rhyolite, *J. Volcanol. Geotherm. Res.*, *60*(2), 179–191.

Bagdassarov, N. S., and D. B. Dingwell (1992), A rheological investigation of vesicular rhyolite, *J. Volcanol. Geotherm. Res.*, *50*(3), 307–322.

Bagdassarov, N., A. Dorfman, and D. B. Dingwell (2000), Effect of alkalis, phosphorus, and water on the surface tension of haplogranite melt, *Am. Mineral.*, *85*(1), 33–40.

Bercovici, D., Y. Ricard, and G. Schubert (2001), A two-phase model for compaction and damage: 1. General theory, *J. Geophys. Res.*, *106*(B5), 8887–8906.

Boccaccini, A., and B. Hamann (1999), Review in situ high-temperature optical microscopy, *J. Mater. Sci.*, *34*(22), 5419–5436.

Branney, M. J., and B. P. Kokelaar (2002), *Pyroclastic Density Currents and the Sedimentation of Ignimbrites*, Geol. Soc., London.

Castro, J. M., and D. B. Dingwell (2009), Rapid ascent of rhyolitic magma at Chaitén Volcano, Chile, *Nature*, *461*(7265), 780–783.

Castro, J. M., D. B. Dingwell, A. R. Nichols, and J. E. Gardner (2005a), New insights on the origin of flow bands in obsidian, *Geol. Soc. Am. Spec. Pap.*, *396*, 55–65.

Castro, J. M., M. Manga, and M. C. Martin (2005b), Vesiculation rates of obsidian domes inferred from H_2O concentration profiles, *Geophys. Res. Lett.*, *32*, L21307, doi:10.1029/2005GL024029.
Castro, J. M., B. Cordonnier, H. Tuffen, M. J. Tobin, L. Puskar, M. C. Martin, and H. A. Bechtel (2012), The role of melt-fracture degassing in defusing explosive rhyolite eruptions at volcán Chaitén, *Earth Planet. Sci. Lett.*, *333–334*, 63–69.
Chiang, Y.-M., D. P. Birnie, and W. D. Kingery (1997), *Physical Ceramics*, John Wiley, New York.
Connor, C., P. Lichtner, F. Conway, B. Hill, A. Ovsyannikov, I. Federchenko, Y. Doubik, V. Shapar, and Y. A. Taran (1997), Cooling of an igneous dike 20 yr after intrusion, *Geology*, *25*(8), 711–714.
Cordonnier, B., S. Schmalholz, K. U. Hess, and D. Dingwell (2012), Viscous heating in silicate melts: An experimental and numerical comparison, *J. Geophys. Res.*, *117*, B02203, doi:10.1029/2010JB007982.
Dingwell, D. B. (1996), Volcanic dilemma: Flow or blow?, *Science*, *273*(5278), 1054–1055.
Fluegel, A. (2007), Glass viscosity calculation based on a global statistical modelling approach, *Glass Technol.: Eur. J. Glass Sci. Technol., Part A*, *48*(1), 13–30.
Frenkel, J. (1945), Viscous flow of crystalline bodies under the action of surface tension, *J Phys*, *9*(5), 385–391.
Gardner, J. E., and R. A. Ketcham (2011), Bubble nucleation in rhyolite and dacite melts: Temperature dependence of surface tension, *Contrib. Mineral. Petrol.*, *162*(5), 929–943.
Gonnermann, H. M., and M. Manga (2003), Explosive volcanism may not be an inevitable consequence of magma fragmentation, *Nature*, *426*(6965), 432–435.
Gonnermann, H. M., and M. Manga (2007), The fluid mechanics inside a volcano, *Annu. Rev. Fluid Mech.*, *39*(1), 321–356.
Gottsmann, J., and D. B. Dingwell (2002), The thermal history of a spatter-fed lava flow: The 8-ka pantellerite flow of Mayor Island, New Zealand, *Bull. Volcanol.*, *64*(6), 410–422.
Grunder, A., and J. Russell (2005), Welding processes in volcanology: Insights from field, experimental, and modeling studies, *J. Volcanol. Geotherm. Res.*, *142*(1), 1–9.
Grunder, A. L., D. Laporte, and T. H. Druitt (2005), Experimental and textural investigation of welding: Effects of compaction, sintering, and vapor-phase crystallization in the rhyolitic Rattlesnake Tuff, *J. Volcanol. Geotherm. Res.*, *142*(1–2), 89–104.
Hess, K. U., and D. B. Dingwell (1996), Viscosities of hydrous leucogranitic melts: A non-Arrhenian model, *Am. Mineral.*, *81*(9–10), 1297–1300.
Hess, K.-U. (1996), Zur Temperaturabhängigkeit der Viskosität von haplogranitischen Schmelzen, PhD thesis, University of Bayreuth.
Kingery, W. D., and M. Berg (1955), Study of the initial stages of sintering solids by viscous flow, evaporation-condensation, and self-diffusion, *J. Appl. Phys.*, *26*(10), 1205–1212.
Klug, C., and K. V. Cashman (1996), Permeability development in vesiculating magmas: Implications for fragmentation, *Bull. Volcanol.*, *58*(2–3), 87–100.
Kolzenburg, S., M. J. Heap, Y. Lavallee, J. K. Russell, P. G. Meredith, and D. B. Dingwell (2012), Strength and permeability recovery of tuffisite-bearing andesite, *Solid Earth*, *3*(2), 191–198.
Kueppers, U., C. Cimarelli, K. U. Hess, J. Taddeucci, F. B. Wadsworth, and D. B. Dingwell (2014), The thermal stability of Eyjafjallajökull ash versus turbine ingestion test sands, *J. Appl. Volcanol.*, *3*, 4.
Lara, C., M. Pascual, M. Prado, and A. Duran (2004), Sintering of glasses in the system Al_2O_3–BaO–SiO_2 studied by hot-stage microscopy, *Solid State Ionics*, *170*(3), 201–208.
Laumonier, M., L. Arbaret, A. Burgisser, and R. Champallier (2011), Porosity redistribution enhanced by strain localization in crystal-rich magmas, *Geology*, *39*(8), 715–718.
Lavallée, Y., P. Benson, M. Heap, K.-U. Hess, B. Schillinger, P. Meredith, and D. B. Dingwell (2013), Reconstructing magma failure and the degassing network of dome-building eruptions, *Geology*, *41*, 515–518.
Lavallée, Y., T. Hirose, J. Kendrick, S. De Angelis, L. Petrakova, A. Hornby, and D. Dingwell (2014), A frictional law for volcanic ash gouge, *Earth Planet. Sci. Lett.*, *400*, 177–183.
Mackenzie, J., and R. Shuttleworth (1949), A phenomenological theory of sintering, *Proc. Phys. Soc. Sect. B*, *62*(12), 833.
Michaut, C., D. Bercovici, and R. S. J. Sparks (2009), Ascent and compaction of gas rich magma and the effects of hysteretic permeability, *Earth Planet. Sci. Lett.*, *282*(1), 258–267.
Michol, K., J. Russell, and G. Andrews (2008), Welded block and ash flow deposits from Mount Meager, British Columbia, Canada, *J. Volcanol. Geotherm. Res.*, *169*(3), 121–144.
Mueller, R., M. Eberstein, S. Reinsch, W. Schiller, J. Deubener, and A. Thiel (2007), Effect of rigid inclusions on sintering of low temperature co-fired ceramics, *Phy. Chem. Glasses-Eur. J. Glass Sci. Technol. Part B*, *48*(4), 259–266.
Mueller, S., O. Melnik, O. Spieler, B. Scheu, and D. B. Dingwell (2005), Permeability and degassing of dome lavas undergoing rapid decompression: An experimental determination, *Bull. Volcanol.*, *67*(6), 526–538.
Mueller, S., B. Scheu, O. Spieler, and D. B. Dingwell (2008), Permeability control on magma fragmentation, *Geology*, *36*(5), 399–402.
Okhotin, M. V., and R. I. Tsoi (1952), *Steklo i Keramika* [in Russian], *8*, 3.
Okumura, S., M. Nakamura, T. Nakano, K. Uesugi, and A. Tsuchiyama (2010), Shear deformation experiments on vesicular rhyolite: Implications for brittle fracturing, degassing, and compaction of magmas in volcanic conduits, *J. Geophys. Res.*, *115*, B06201, doi:10.1029/2009JB006904.
Olevsky, E. A. (1998), Theory of sintering: From discrete to continuum, *Mater. Sci. Eng.: R: Rep.*, *23*(2), 41–100.
Pascual, M., L. Pascual, and A. Dura'n (2001), Determination of the viscosity-temperature curve for glasses on the basis of fixed viscosity points determined by hot stage microscopy, *Phys. Chem. Glasses-Europ. J. Glass Sci. Technol. Part B*, *42*(1), 61–66.
Pascual, M., A. Durán, M. Prado, and E. Zanotto (2005), Model for sintering devitrifying glass particles with embedded rigid fibers, *J. Am. Ceram. Soc.*, *88*(6), 1427–1434.
Prado, M. O., C. Fredericci, and E. D. Zanotto (2003), Isothermal sintering with concurrent crystallization of polydispersed soda–lime–silica glass beads, *J. Non Cryst. Solids*, *331*(1), 145–156.
Prado, M., E. Dutra Zanotto, and R. Müller (2001), Model for sintering polydispersed glass particles, *J. Non Cryst. Solids*, *279*(2), 169–178.
Quane, S. L., and J. Russell (2005a), Welding: Insights from high-temperature analogue experiments, *J. Volcanol. Geotherm. Res.*, *142*(1), 67–87.
Quane, S. L., and J. Russell (2006), Bulk and particle strain analysis in high-temperature deformation experiments, *J. Volcanol. Geotherm. Res.*, *154*(1), 63–73.
Quane, S. L., and J. K. Russell (2003), Rock strength as a metric of welding intensity in pyroclastic deposits, *Eur. J. Mineral.*, *15*(5), 855–864.
Quane, S. L., and J. K. Russell (2005b), Ranking welding intensity in pyroclastic deposits, *Bull. Volcanol.*, *67*(2), 129–143.
Quane, S. L., J. K. Russell, and E. A. Friedlander (2009), Time scales of compaction in volcanic systems, *Geology*, *37*(5), 471–474.
Ragan, D., and M. Sheridan (1972), Compaction of the bishop Tuff, California, *Geol. Soc. Am. Bull.*, *83*(1), 95–106.
Rahaman, M. N., L. C. De Jonghe, G. W. Scherer, and R. J. Brook (1987), Creep and densification during sintering of glass powder compacts, *J. Am. Ceram. Soc.*, *70*(10), 766–774.

Ross, C. S. (1960), Ash-flow tuffs: Their origin, geologic relations and identification. [Available from New Mexico Bureau of Mines and Mineral Resources.]
Russell, J. K., and S. L. Quane (2005), Rheology of welding: Inversion of field constraints, *J. Volcanol. Geotherm. Res.*, *142*(1), 173–191.
Scherer, G. W. (1977), Sintering of low-density glasses: I. Theory, *J. Am. Ceram. Soc.*, *60*(5–6), 236–239.
Scherer, G. W. (1986), Viscous sintering under a uniaxial load, *J. Am. Ceram. Soc.*, *69*(9), C-206–C-207.
Scherer, G. W., and D. L. Bachman (1977), Sintering of low-density glasses: II. Experimental study, *J. Am. Ceram. Soc.*, *60*(5–6), 239–243.
Schipper, C. I., J. M. Castro, H. Tuffen, M. R. James, and P. How (2013), Shallow vent architecture during hybrid explosive–effusive activity at Cordón Caulle (Chile, 2011–12): Evidence from direct observations and pyroclast textures, *J. Volcanol. Geotherm. Res.*, *262*, 25–37.
Sigurdsson, H., B. Houghton, H. Rymer, J. Stix, and S. McNutt (1999), *Encyclopedia of Volcanoes*, Academic Press, Waltham, Mass.
Smith, R. L. (1960), *Zones and Zonal Variations in Welded Ash Flows*, USGS Professional Paper 354-F.
Smith, R. L., and R. A. Bailey (1966), The Bandelier Tuff: A study of ash-flow eruption cycles from zoned magma chambers, *Bull. Volcanol.*, *29*(1), 83–103.
Soares, V. O., R. C. Reis, E. D. Zanotto, M. J. Pascual, and A. Duran (2012), Non-isothermal sinter-crystallization of jagged Li_2O–Al_2O_3–SiO_2 glass and simulation using a modified form of the Clusters model, *J. Non Cryst. Solids*, *358*(23), 3234–3242.
Song, W., K. U. Hess, D. E. Damby, F. B. Wadsworth, Y. Lavallée, C. Cimarelli, and D. B. Dingwell (2014), Fusion characteristics of volcanic ash relevant to aviation hazards, *Geophys. Res. Lett.*, *41*, 2326–2333, doi:10.1002/2013GL059182.
Sparks, R. S. J., S. R. Tait, and Y. Yanev (1999), Dense welding caused by volatile resorption, *J. Geol. Soc.*, *156*(2), 217–225.
Spieler, O., B. Kennedy, U. Kueppers, D. B. Dingwell, B. Scheu, and J. Taddeucci (2004), The fragmentation threshold of pyroclastic rocks, *Earth Planet. Sci. Lett.*, *226*(1), 139–148.
Stasiuk, M. V., J. Barclay, M. R. Carroll, C. Jaupart, J. C. Ratté, R. S. J. Sparks, and S. R. Tait (1996), Degassing during magma ascent in the Mule Creek vent (USA), *Bull. Volcanol.*, *58*(2–3), 117–130.
Stevenson, R., N. Bagdassarov, and C. Romano (1997), Vesiculation processes in a water-rich calc-alkaline obsidian, *Earth Planet. Sci. Lett.*, *146*(3), 555–571.
Sumner, J., S. Blake, R. Matela, and J. Wolff (2005), Spatter, *J. Volcanol. Geotherm. Res.*, *142*(1), 49–65.
Tuffen, H., and D. Dingwell (2005), Fault textures in volcanic conduits: Evidence for seismic trigger mechanisms during silicic eruptions, *Bull. Volcanol.*, *67*(4), 370–387.
Tuffen, H., D. B. Dingwell, and H. Pinkerton (2003), Repeated fracture and healing of silicic magma generate flow banding and earthquakes?, *Geology*, *31*(12), 1089–1092.
Tuffen, H., R. Smith, and P. R. Sammonds (2008), Evidence for seismogenic fracture of silicic magma, *Nature*, *453*(7194), 511–514.
Uhlmann, D., L. Klein, and R. Hopper (1975), Sintering, crystallization, and breccia formation, *The Moon*, *13*(1–3), 277–284.
Vasseur, J., F. B. Wadsworth, Y. Lavallée, K. U. Hess, and D. B. Dingwell (2013), Volcanic sintering: Timescales of viscous densification and strength recovery, *Geophys. Res. Lett.*, *40*, 5658–5664, doi:10.1002/2013GL058105.
Wilding, M., S. Webb, D. Dingwell, G. Ablay, and J. Marti (1996), Cooling rate variation in natural volcanic glasses from Tenerife, Canary Islands, *Contrib. Mineral. Petrol.*, *125*(2–3), 151–160.
Wright, H. M., and K. V. Cashman (2014), Compaction and gas loss in welded pyroclastic deposits as revealed by porosity, permeability, and electrical conductivity measurements of the Shevlin Park Tuff, *Geol. Soc. Am. Bull.*, *126*(1–2), 234–247.